



Enhanced activity and stability of Ru-TiO₂ rutile for liquid phase ketonization



Nicolás Aranda-Pérez, M. Pilar Ruiz, Javier Echave, Jimmy Faria*

Abengoa Research, Campus Palmas Altas, C/Energía Solar 1, 41014 Seville, Spain

ARTICLE INFO

Article history:

Received 9 August 2016

Received in revised form 5 October 2016

Accepted 23 October 2016

Available online 24 October 2016

Keywords:

Ketonization

Titanium dioxide

Hydrothermal stability

Hydrophobicity

ABSTRACT

Stabilization of oxygen vacancies on metal oxides (e.g. TiO₂) in liquid phase is an important challenge for the utilization of these materials in artificial photosynthesis, environmental remediation and biomass conversion. To create materials with low-energy barriers for vacancies formation and high stability in aqueous environments, we have developed partially hydrophobic (contact angle $\geq 90^\circ$) TiO₂ rutile decorated with Ru nanoparticles. Negligible catalytic activity was observed when hydrophilic (contact angle 51°) 5 wt.% Ru/TiO₂ anatase was utilized in hot liquid water, while amphiphilic 5 wt.% Ru/TiO₂ rutile (contact angle $\sim 90^\circ$) retained its catalytic activity. Fine-control of crystalline structure (lattice matching) of TiO₂ and Ru allowed us to accelerate the rate of reaction, while the high surface hydrophobicity of the support enabled the stabilization of Ti³⁺ cations in aqueous and organic environments.

© 2016 Published by Elsevier B.V.

1. Introduction

Biomass is the largest reservoir of renewable carbon on the planet reaching annual production rates of 170 billion metric tons [1], and the potential of replacing 27% of the annual world total transport fuel demand (i.e. diesel, kerosene and jet fuel), which could avoid around 2.1 gigatonnes (Gt) of CO₂ emissions [2]. However, harvesting and transforming the biomass into liquid transportation fuels and chemicals is not simple [3]. It requires complex chemical transformation steps that can reduce the oxygen content of the biomass, while preserving the carbon and hydrogen [4–6]. The liquefaction of biomass via fast pyrolysis is an interesting alternative as the liquid product and energy density is maximized while the oxygen-to-carbon ratio is reduced. The resulting pyrolysis oil (bio-oil) is a complex mixture of water and oxygenated compounds (e.g. short acids, aldehydes, anhydrosugars, furans, and phenolics). This bio-oil can be used directly or processed for heat, power, biofuels, and chemicals [7–9]. In order to make a fungible fuel the pyrolysis oil must undergo a catalytic upgrading process to reduce the excess oxygen and increase C–C length of the small molecules, while preserving the energy content [10–14].

To accomplish this goal, the small acids, which can account up to 30% of the aqueous phase, must be transformed into larger hydrocarbons before undergoing hydrogenation to avoid the formation of

low-value light gases (e.g. methane, ethane) during hydrotreating. Ketonization of the acids can be employed to reduce the oxygen content by elimination of CO₂ and H₂O, while making a ketone that can serve as an alkylation agent of aromatics downstream [15]. Additionally, the presence of water in high concentrations makes unavoidable the development of stable catalytic materials that can operate under hydrothermal stress [16,17].

On transition metal oxides surfaces, decarboxylative C–C coupling or ketonization reaction takes place on coordinatively unsaturated metal cations or oxygen vacancies where the carboxylates are adsorbed to form intermediate species that lead to the formation of ketones [18,19]. The catalytic activity of the metal oxides is strongly dependent on the presence of surface metal cations/oxygen anions pairs that act as Lewis acids and bases towards the carboxylates. On metal oxides with reducible properties (i.e. TiO₂, CeO₂, ZrO₂), it is possible to generate oxygen vacancies at temperatures above 300 °C for ketonization reactions in vapor phase [15]. At lower temperatures, however, the ketonization reaction does not occur on bare amphoteric oxides as the unsaturated metal cations are not formed [20]. One alternative to promote this process is to add doping agents (e.g. Na, K, Cs) [21] and metals with high hydrogen-dissociation activity [20,22,23]. On metal oxides doped with reducible metals, e.g. Ru/TiO₂, it is possible to increase significantly the ketonization rate by creating additional active sites upon reduction in H₂ [20,22,24]. For instance, in bio-oil upgrading, where the ketonization of short-chain acids allows oxygen removal and C–C chain growth with zero consumption of hydrogen, it is particularly important to perform the reaction at

* Corresponding author.

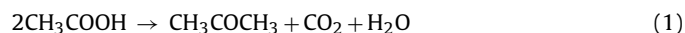
E-mail address: ing.jimmyfaria@gmail.com (J. Faria).

mild temperatures (<250 °C) to avoid secondary reactions [25,26]. Operating in aqueous environments at moderate temperatures (>150 °C) is remarkably difficult due to the structural collapse of the metal oxide [27] and competitive adsorption of water onto unsaturated metal cations, like partially unsaturated Ti cations (i.e. Lewis acid sites) [28–30].

A detailed experimental study of the mechanisms controlling the stability of zeolite catalysts in liquid water revealed that defects on the crystalline structure are the controlling factor [31]. The defective sites, typically hydroxylated metal-oxygen bonds, serve as nucleation sites for the initiation of the degradation process [32]. The stability of the zeolite is dramatically improved by either functionalization of these OH-functionalities by silylation with organosilanes [16] or synthesis in fluorinated media to create near-perfect crystalline structures. [32–35] The surface wettability of amphoteric metal oxides like TiO₂ is far more complex than conventional metal oxides and zeolites, as these materials can reversibly switch from hydrophobic to superhydrophilic upon exposure to UV-light [36]. The formation of surface hydroxyl groups on Ti³⁺ cations, generated by the UV-Light, increases the surface hydrophilicity. More recently, X. Feng et al. [37] reported that it is possible to achieve switchable superhydrophobicity on TiO₂ rutile nanorods films, as a result of the combination of micro- and nanoscale hierarchical surface structures, the orientation of the crystal planes and the surface photosensitivity.

Inspired on this previous research, we have developed a material that combines the high activity of TiO₂ rutile-ruthenium interface with the hydrophobic modification of the surface by thermal dehydroxylation. To investigate the interaction of the crystalline phases of TiO₂ and the effect of hydrophobicity, three catalysts composed of Ru supported on TiO₂ anatase, TiO₂ P25 (mixture of anatase:rutile 80:20 in weight), and TiO₂ rutile were synthesized. A detailed characterization of the different materials and catalysts stability studies in aqueous phase enabled the identification of properties-structure-performance relationships. As a showcase we have selected the ketonization reaction of acetic acid, which is present in high-concentrations in bio-oil mixtures and is one of the main contributors to the corrosiveness and instability of pyrolysis oil [7,9,38].

The simplified ketonization reaction of acetic acid is the following:



Experimental studies have shown that ketonization rate of reaction is strongly dependent on the number of α -hydrogen of the molecule [39–41]. That is on carboxylic acids with higher number of α -hydrogen the faster the reaction rate. In addition, transition state analysis of kinetic data obtained for the ketonization of carboxylic acids with different chain-length suggested that this reaction proceeds via a β -ketoacid intermediate. The reaction rate significantly decreases when long-chain carboxylic acids were reacted as the C–C coupling reaction was hindered by bulkier alkyl-groups [22]. Density Functional Theory study on ZrO₂ slab showed that the formation of ketones through a concerted mechanism is kinetically unfavorable. In contrast, the pathway involving a α -hydrogen abstraction step had much lower activation energy, due to the formation of a highly reactive nucleophile that reacts with a nearby carboxylate molecule to produce a β -ketoacid intermediate that produces the ketone upon decarboxylation [42]. Based on this we have decided to use as a probe molecule acetic acid, which is a molecule containing three α -hydrogen.

2. Materials and methods

2.1. Catalyst synthesis

First, three different commercial TiO₂ were selected attending its phase composition: anatase (TiO₂ G5), rutile (TiO₂ Rutile), and anatase/rutile in a proportion of 80/20 (TiO₂ P25). TiO₂ P25 and TiO₂ G5 were kindly provided by Evonik Industries and rutile was purchased to Sigma Aldrich. The three catalysts of the study were synthesized by excess volume impregnation of the Ru precursor on the different TiO₂ supports. The Ru loading was 5 wt.% using Ru (III) Chloride precursor (Sigma Aldrich, 99.98%). The required amount of the metal precursor was dissolved in deionized water and left for solution for 4 h; subsequently TiO₂ was added and kept under stirring (500 rpm) overnight. Afterwards, evaporation of water was performed by heating at 150 °C for 3 h. Once the impregnation is accomplished, the catalyst was dried at 100 °C overnight and finally calcined at 400 °C for 4 h with a heating ramp of 2 °C/min. The same preparation procedure was followed for all the samples. In this work the catalysts are labeled as Ru/TiO₂ anatase, Ru/TiO₂ rutile and Ru/TiO₂ P25.

2.2. Catalyst characterization

The catalysts were characterized by micro-fluorescence of X-Rays (MXRF), transmission electron microscopy (TEM), X-ray diffraction (XRD), N₂-physisorption, temperature-programmed reduction (TPR), and temperature programmed desorption of NH₃ (NH₃-TPD), and powder contact angle.

2.2.1. X-rays microfluorescence (XRMF)

Compositional analysis of the catalysts was performed employing a microfluorescence X-Ray spectrometer Eagle-III from EDAX employing a 40 W Rh X-Ray tube. The detection system employed an 80 mm² Lithium-drifted Silicon crystal liquid N₂ cooled with a Be window that can allow Na and U simultaneous detection with a resolution of <150 eV for MnK α at 5000 counts per second (CPS) and <185 eV for MnK α at 15,000 CPS. The optics of the Eagle-III consisted on a mono-capillary system operating at 300 μ m and open aperture of 2 mm spot. The powder samples were placed in the sample holder and introduced as synthesized inside the analysis chamber. The analysis was performed using a total data acquisition time of approximately 15 s on a 300 μ m scanning area.

2.2.2. High angle annular dark-field scanning transmission electron microscopy (HAADF), high-resolution transmission electron microscopy and energy dispersive X-ray spectroscopy (HR-TEM-EDS)

High angle annular dark-field scanning transmission electron microscopy (HAADF-STEM) and high-resolution transmission electron microscopy (HRTEM) was carried out using a FEI Tecnai F30, operated at 300 kV equipped with a Gatan CCD camera, an EDS (EDAX) detector and a Gatan Tridiem Energy Filter. Each sample was prepared by sonicating in *n*-butanol to improve the dispersion of the particles. The solution was dropped onto a holey carbon coated 300 mesh copper grid.

2.2.3. X-ray diffraction (XRD)

XRD analysis was carried out on a D8I Bruker for dust samples with incident slits with Cu anode. The data were collected in an angle range 0–45°. A semi-quantitative method was used to determine the crystalline structure of TiO₂ comparing to Corindon data-base.

2.2.4. N₂-Physisorption

BET surface area, pore size and volume were measured using N₂ physisorption at liquid nitrogen temperature on a Micromeritics ASAP 2020C. Degasification was performed at a temperature of 200 °C for 4 h.

2.2.5. Temperature programmed reduction (TPR)

TPR analysis of 100 mg of the catalysts were conducted in Autochem 2920 using a gas mixture of 10% H₂ in Ar at a flow rate of 30 sccm with a linear heating ramp of 5 °C/min up to 900 °C and holding time of 1 min. H₂ consumption was determined by a thermal conductivity detector.

2.2.6. Ammonia temperature programmed desorption (NH₃-TPD)

NH₃-TPD was carried out on Autochem 2920 using a gas mixture of 15% NH₃ in He. The surface was firstly clean with He, then it was reduced in 50 sccm of H₂ at 230 °C during 3 h to replicate reduction conditions, then it was cleaned again with He at 230 °C to evaporate any H₂O formed. Once 35 °C was reached, 15% NH₃/He was passed through the sample for 60 min in which it was chemisorbed. Finally, a temperature ramp of 10 °C/min up to 900 °C was programmed to study the desorption profile, which is related to the concentration of exposed cations on the catalyst. Total acidity was measured by integrating the area under the curve of NH₃-TPD.

2.2.7. Powder contact angle (PCA)

Powder contact angle was measured using DCAT21 from Dataphysics. The samples were measured first with *n*-hexane for calibration and then with deionized water.

2.3. Ketonization experiments

Ketonization reactions were carried out in a 150 mL batch reactor (Berghof BR-100) with a Teflon liner of 100 mL to avoid corrosion of the reactor. A scheme of the experimental setup is shown in Fig. S1. Firstly, 200 mg of catalyst and 65 mL of *n*-hexane (VWR, 99%) or deionized water (depending on the experiment), were loaded on the liner. In a first stage, the catalyst was reduced by placing the insert on the reactor and pressurizing, after purge with N₂, with 30 bar of H₂ stirring at 750 rpm. The reduction was conducted at 230 °C and the pressure increased autogenously (60 bar) for 3 h. After cooling the reactor to room temperature, the H₂ was purged and N₂ at 5 bar was introduced into the reactor. Then after a heating ramp of 2 h, the target temperature of the reaction was reached (200 °C, 210 °C, 220 °C depending on the experiment), at this moment, which indicates the starting time of the reaction, 7 mL of acetic acid were injected through an injection tank, and the pressure was increased to 50 bar. Magnetic stirring was kept at 750 rpm to maintain the catalyst suspended to avoid mass transfer limitations. Reactions were run for 15 min, 30 min, 1 h and 2 h to establish the kinetics for each of the temperatures and time. Once the time of the reaction was completed, the reactor was quickly cool down to 10 °C. Then, it was depressurized to ambient pressure and two liquid aliquots were taken for gas chromatography (GC) analysis and quantification. An Agilent Technologies 7890C GC equipped with autosampler and autoinjector was used for quantification of the products and reactants. The column used for separating the constituents was HP-5 (30 m × 0.32 mm, 0.25 μm). The mass balance for these experiments was typically close to about 95%.

Recycling experiments were conducted to study the catalyst stability in the ketonization reaction, following the same procedure aforementioned. After each reaction cycle the reactor effluent was filtered in a Nylon filter of 0.2 μm and dried overnight at 80 °C. The dried catalyst was weighted and placed back inside the reactor for the next reaction experiment. To make the experiments compar-

able, the catalyst to feed ratio (m/v) was maintained constant (acetic acid:catalyst 1:0.61).

3. Results and discussion

3.1. Characterization results

3.1.1. X-rays microfluorescence (XRMF)

The catalyst samples were characterized by X-rays microfluorescence (XRMF) to determine the exact loading of ruthenium achieved after impregnation. The powder samples were placed in the sample holder and introduced "as synthesized" inside the analysis chamber. In Table 1 are summarized the compositional results obtained for the three catalysts samples. The results indicate that the loading of ruthenium varied from 3.9 to 6.9 wt.%. This value was close to the calculated loading of 5 wt.% of Ru on TiO₂. This information was employed to determine the degree of exact degree of reduction of the metal and support in the temperature programmed reduction experiments in Section 3.1.5. While the real loadings, ranging from 3.9 to 6.9 wt.% of Ru on TiO₂, were employed in the calculation of the extent of reduction of the catalyst the theoretical value of 5 wt.% metal loading was employed in the data presentation and discussions for clarity and homogeneity.

3.1.2. High angle annular dark-field scanning transmission electron microscopy (HAADF), high-resolution transmission electron microscopy and energy dispersive X-ray spectroscopy (HR-TEM-EDS)

High-resolution transmission electron microscopy (TEM) characterization of the samples revealed significant differences in geometry of TiO₂ and size of Ru nanoparticles (see Figs. 1 and 2 a–c). On 5 wt.% Ru/TiO₂ rutile catalyst, highly uniform hexagonal particles of TiO₂ were observed with average particle size of 44 ± 11 nm, while anatase and P25 catalysts were composed of spherical particles of 30 ± 8 nm and 33 ± 9 nm, respectively (Fig. 1). Notably, the particle size distribution of anatase and P25 were significantly narrower than the one obtained for anatase.

Energy dispersive X-ray (EDX) of the samples allowed the identification of the Ru nanoparticles (Fig. 2a-ii, b-ii, and c-ii). To properly determine the particle size the three catalysts a significant number of images at low and high magnification (>60 images) were processed. First, the identification of the ruthenium particles was performed using EDX, then the particles were sized (see Fig. 2). On anatase, Ru nanoparticles had an average particle size of 6.9 ± 3.7 nm with a wide distribution of particles (Table 2); while on P25 the distribution of Ru particles size was narrower with an average particle size of 4.2 ± 1.6 nm. In sharp contrast, TiO₂ rutile was able to stabilize smaller Ru nanoparticles of 3.1 ± 1.1 nm with a narrower distribution.

Table 1

X-ray microfluorescence compositional analysis of the different catalysts.

| Catalyst | Ru (wt.%) | Error% | Ti (wt.%) | Error% |
|--------------------------------|-----------|--------|-----------|--------|
| 5% Ru/TiO ₂ anatase | 3.9% | 0.2% | 96% | 1.6% |
| 5% Ru/TiO ₂ P25 | 6.9% | 0.3% | 93% | 1.5% |
| 5% Ru/TiO ₂ rutile | 6.1% | 0.2% | 94% | 1.6% |

Table 2

Ru particle size and dispersion calculated from TEM.

| Sample | Average size (nm) | Metal dispersion (%) |
|--------------------------------|-------------------|----------------------|
| 5% Ru/TiO ₂ Anatase | 6.9 ± 3.7 | 12 |
| 5% Ru/TiO ₂ P25 | 4.2 ± 1.6 | 24 |
| 5% Ru/TiO ₂ Rutile | 3.1 ± 1.1 | 31 |

Note: Metal dispersion has been estimated from TEM images following the method described elsewhere [52].

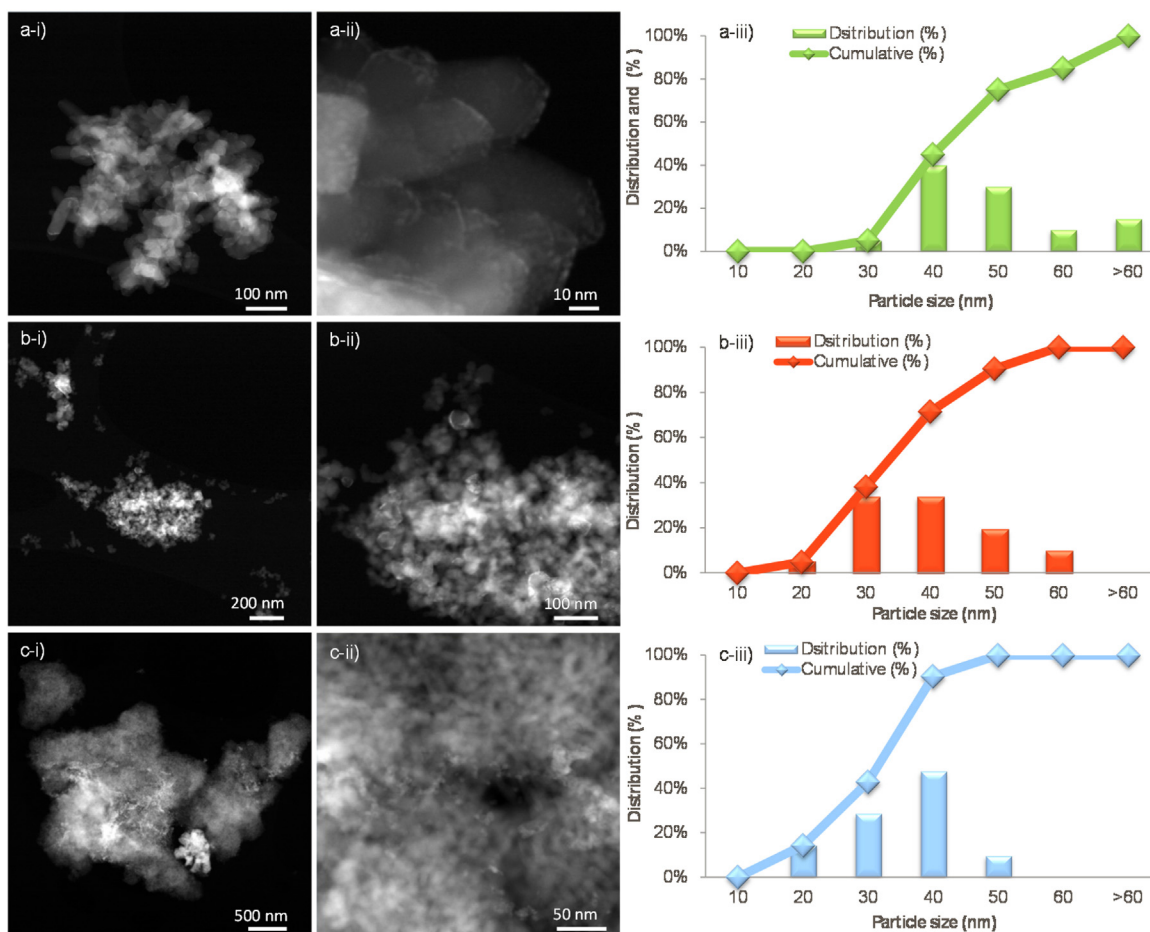


Fig. 1. Structural of 5 wt.% Ru supported on TiO₂ rutile (a), P25 (b), and anatase (c) obtained by scanning transmission electron microscopy (STEM) at two magnifications (i-ii). Particle size distribution obtained from HRTEM images of TiO₂ rutile (a-iii green), P25 (red-iii b), and anatase (blue-iii). (For interpretation of the references to color in this figure legend, the reader is referred to the web version of this article.)

This enhancement of Ru dispersion on rutile can be explained in terms of metal-support interactions [43]. The differences in crystallographic and electronic structure between rutile and anatase are key to rationalize the particle size distribution. Initially, ruthenium clusters were deposited using a wetness impregnation method under the same operating conditions. After the impregnation the RuCl₃ deposited on the samples is decomposed at high temperatures in the presence of air. This process leads to the formation of RuO₂ clusters with rutile structure on the surface of the TiO₂. Here, the interfacial lattice matching of RuO₂ and TiO₂ favors the formation of Ru-O-Ti bonds reducing the mobility of Ru clusters during calcination at 400 °C [43–48]. While it is possible that under reducing conditions at high temperature ruthenium particles undergo particle sintering [49], previously reported data has shown that small metal clusters, such as Pt, can be effectively stabilized on surface defects or vacant sites of TiO₂ [50]. The authors showed that on TiO₂ P25 the Pt clusters preferentially grow on the rutile surface, creating an uneven distribution of particles. Detailed ab-initio pseudopotential calculations for Pt and Pt₂ on the stoichiometric and reduced TiO₂ surfaces and oxygen vacancies showed that in rutile the lower formation energies of oxygen vacancies (V_o) and stronger interaction of Pt with V_o sites favored the stabilization of a larger fraction of metal cluster with a smaller size on the rutile surface, compared to anatase [51]. Hence, it is possible that on Ru/TiO₂ rutile surface the stabilization of smaller particles is due to a combination of the lattice matching of RuO₂ and TiO₂ rutile during calcination and the metal-vacancy interaction during the

reduction process. This will be in line with the trend of dispersion observed, in which Ru cluster sizes were increasing monotonically from rutile to P25 to anatase. Although Ru/TiO₂ rutile is the catalyst with the smallest surface area (23 m²/g), compared to Ru/TiO₂ anatase (114 m²/g), its ruthenium dispersion is the highest among the three catalyst samples.

The metal dispersion was estimated using a semi-empirical correlation of the particle size of metal clusters obtained by HRTEM to dispersion published by Larson [52]. Previous work has demonstrated the validity of this approach [53–56]. Dalla and Taylor pioneering work in correlating metal dispersion and H₂ chemisorption showed that it is possible to determine the metal particle size from the hydrogen chemisorption on reduced metals. For instance, X. Shen et al. [55] reported good agreement between the measurements of metal dispersion of ruthenium on TiO₂ by hydrogen chemisorption and two indirect characterization techniques like X-ray diffraction line broadening and Transmission Electron Microscopy. Similarly, J. Okal et al. [56] observed that dispersion of ruthenium nanoparticles on alumina determined by hydrogen chemisorption and TEM characterization methods were in good agreement, except in those cases where impurities were present. Other methods, like the one developed by G. Bergeret and P. Galletot allow the estimation of metal dispersion based on particle size [57]. This method, however, employs the atomic area of the topmost surface atoms, which is a parameter rather difficult to determine. The technique herein employed is an improved version of the previously reported alternative as it takes into consideration

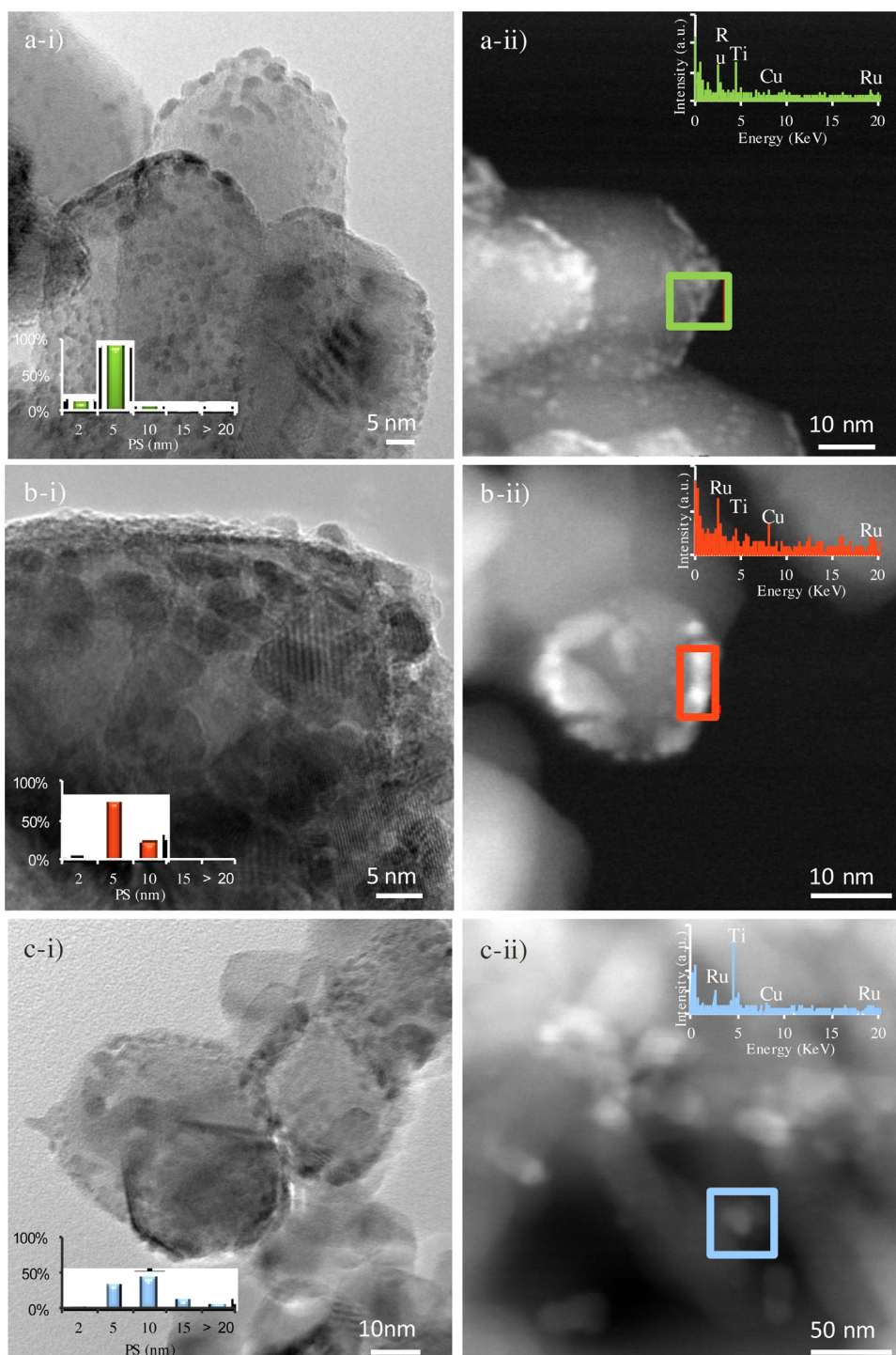


Fig. 2. Structural and chemical characterization of 5 wt.% Ru supported on TiO₂ rutile (a), TiO₂ P25 (b), and TiO₂ anatase (c) obtained by high-resolution transmission electron microscopy (HRTEM) (i) and scanning transmission electron microscopy (STEM) (ii). Inset graphs on figures a-i, b-i, and c-i correspond to particle size distribution of ruthenium on TiO₂ rutile (green), P25 (red), and anatase (blue). Insets on figures a-ii, b-ii, and c-ii corresponded to energy dispersive X-Ray (EDX) of highlighted regions showing peaks of Ti, Ru, and Cu (Cu from TEM-grid). (For interpretation of the references to color in this figure legend, the reader is referred to the web version of this article.)

the possible deviations related to the estimation of the atomic area of the surface atoms. Table 2 summarizes the results of the metal dispersion. Notably, the catalyst supported on TiO₂ rutile presented the highest Ru dispersion, with a value of 31%, while the anatase-supported catalyst presented the lowest value (14%) followed by P25 with 24%.

3.1.3. X-ray diffraction (XRD)

X-ray diffraction characterization of the samples (Fig. 3a) showed high-degree of crystallinity, evidenced by sharp intense diffraction peaks, corresponding to anatase (♦) and rutile (●). In Ru/P25 catalyst, the fingerprints of both anatase and rutile were observed as this material is a mixture of anatase:rutile 80:20 in weight. On Ru/TiO₂ anatase the larger particle size of RuO₂ allowed

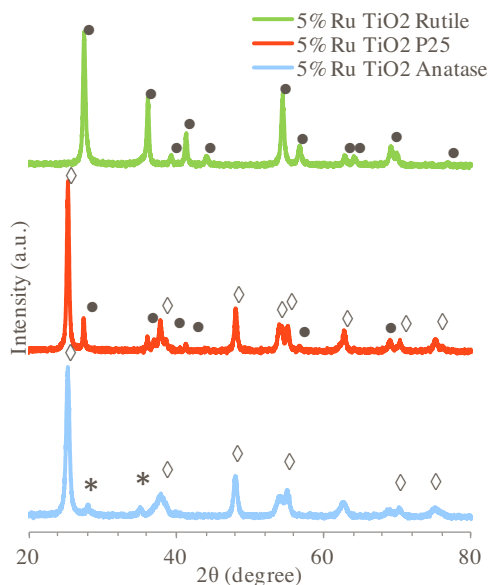


Fig. 3. X-ray diffraction patterns of the unreduced Ru catalysts showing the characteristic fingerprints of TiO₂ (●) rutile, (◇) anatase, and (*) RuO₂.

Table 3
BET surface area of the supports and catalysts.

| Sample | BET Surface Area (m ² /g) | Pore volume (cm ³ /g) | Pore size (Å) |
|--------------------------------|--------------------------------------|----------------------------------|---------------|
| TiO ₂ Anatase | 114 | 0.369 | 129 |
| 5%/Ru/TiO ₂ Anatase | 93 | 0.333 | 143 |
| TiO ₂ P25 | 57 | 0.128 | 94 |
| 5%/Ru/TiO ₂ P25 | 47 | 0.189 | 159 |
| TiO ₂ Rutile | 23 | 0.144 | 247 |
| 5%/Ru/TiO ₂ Rutile | 25 | 0.150 | 243 |

the identification of RuO₂ (*) fingerprints. The peaks observed at 28, 35 and 55° can be indexed to the planes (110), (101) and (211) of tetragonal RuO₂, respectively (JCPDS 21-1172) [58]. The absence of RuO₂ on rutile and P25 based catalysts can be attributed to the high dispersion of Ru clusters and overlaying of diffraction peaks from TiO₂ rutile. Notably, the size of Ru clusters was independent of the support surface area.

3.1.4. N₂-Physisorption

Textural characterization of the catalysts by N₂-physisorption (Table 3) revealed that on Ru supported TiO₂ anatase the specific surface area was significantly larger (93 m²/g) than the one observed on Ru supported on P25 (57 m²/g) and rutile (25 m²/g). The loss in surface upon deposition of Ru clusters can be attributed to the structural rearrangement of the metal oxide surface, which leads to the pore collapse [59].

The Barrett-Joyner-Halenda (BJH) analysis of desorption isotherms of N₂ (Fig. 4a-b) indicated that all of the materials were primarily mesoporous. On anatase and P25 based catalysts a narrow pore size distribution was observed with average pore size, determined by the Brunauer, Emmett and Teller method (BET), of 143 and 159 Å, respectively (Table 3). On rutile catalyst the pore size distribution was significantly wider with pores ranging from 20 to 1000 Å with an average pore size of 247 Å, which could be indicative of fractal-like macro- and meso- porosity [60–62].

3.1.5. Temperature programmed reduction (TPR)

Temperature programmed reduction was employed to determine the reducibility of the different catalysts (Fig. 5). The peaks were fitted using up to six Gaussian curves with the idea of facil-

itate the analysis of the results. Notably, it is possible to identify a low-temperature reduction peak (1) of Ru at 80–90 °C for the 5% wt. Ru supported on TiO₂ rutile. A series of convoluted peaks were observed between 100 °C and 250 °C for all the catalysts. On Ru/anatase catalyst, a peak at 350 °C appeared. Finally, a broad peak (2) was observed starting at 450 °C and extending up to 650 °C on Ru/rutile catalyst. It is interesting to note that on 5% wt. Ru supported on TiO₂ P25 peak 1 and 2 were not observed. Also, on anatase supported catalyst, peak 1 was not observed and peak 2 was slightly shifted to higher temperatures.

The profiles obtained by temperature programmed reduction of the Ru/TiO₂ catalysts showed the presence of multiple reducible species. Previously reported data have shown similar TPR profiles for Ru/TiO₂/C [20]. In that case, however, the presence of high-surface area provided by the activated carbon enabled the stabilization of Ru clusters that were not in contact with TiO₂. The reducibility of these clusters was strongly affected by the particle size of the catalyst. For this reason, they attributed the reduction peaks at 121 and 183 °C to Ruthenium with different particle sizes. The rest of the peaks between 200 and 500 °C were tentatively assigned to reduction of titanium and ruthenium oxides in close interaction, which delayed the reduction of Ru, but enhanced the reduction of TiO₂. This could explain the presence of several reduction peaks at temperatures below 500 °C.

Isothermal reduction experiments performed by J.E. Rekoske and M. A. Barteau [63] demonstrated that the reduction rates and density of surface defects on TiO₂ strongly depend on the crystalline phase. That is on anatase the concentration unsaturated Ti cations is smaller and the rate of reduction are slower than in rutile. These observations are in agreement with Density Functional Theory (DFT) calculations that showed that on rutile the formation energies of oxygen vacancies (V_o) is lower than in anatase [64]. In the case of Ru/TiO₂ anatase, herein reported, the TEM-EDX characterization revealed that in this support the particle size distribution of Ru was significantly larger and wider than the one observed on polymorph P25 and rutile with values of 6.9 ± 3.7, 4.2 ± 1.6, and 3.1 ± 1.1 nm, respectively. Therefore, in the particular case of Ru/TiO₂ anatase it is possible that the TPR peak centered at 350 °C was caused by a combination of different factors, including; larger particle size of ruthenium, lower reducibility of anatase support, and weaker interaction between Ru-TiO₂ surfaces. In the starting material, i.e. TiO₂ P25 (see Fig. S3), the reduction profile is quite different from that observed on Ru/TiO₂ P25. At low temperatures the hydrogen consumption was negligible. A broad peak between 550 and 800 °C was observed, which is in line with previously reported data for TiO₂ [65]. This peak corresponded to reduction of the support at high-temperatures.

On Ru/TiO₂ P25 the reduction peak was shifted to temperatures ranging from 100 to 300 °C that are related to reduction of ruthenium and titanium oxides. The absence of low temperature reduction peaks could be related to the strong influence that the reducibility of the support could exert on the ruthenium nanoparticles as TiO₂ anatase and polymorph P25 (80:20 anatase:rutile) are less reducible than rutile [63].

The extent of reduction of RuO₂ and TiO₂ oxides was determined using the moles of hydrogen consumed on each experiment (see Table 4). The results indicate that in Ru/TiO₂ anatase, P25, and rutile the amount of hydrogen consumed vary significantly with the support with values of 527.1, 196.7, and 457.7 μmol of H₂/g_{ofcatalyst}, respectively. While the hydrogen consumption per mass for anatase was higher than rutile, the H₂ uptakes in terms of surface area followed the opposite trend. For instance, on Ru/TiO₂ rutile the H₂ consumed was 3.2 times larger than in anatase. Notably, the extent of reduction for ruthenium was complete for all the catalysts, while in the case of TiO₂ the degree of reduction

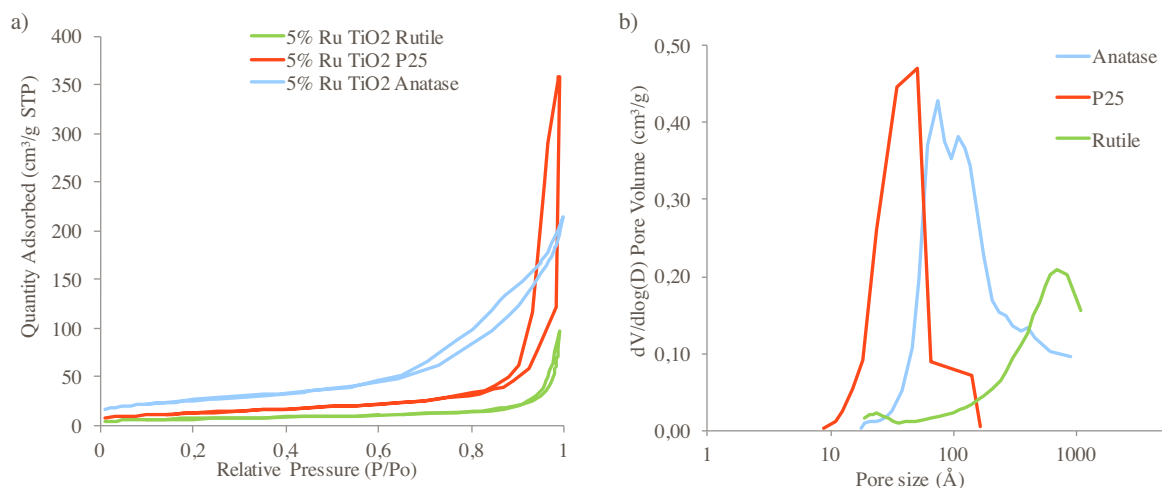


Fig. 4. N₂ adsorption and desorption isotherms and pore size distribution obtained from Barrett-Joyner-Halenda (BJH) Analysis of N₂-desorption isotherms of 5 wt.% Ru supported on TiO₂ rutile (green), P25 (red), and anatase (blue). (For interpretation of the references to color in this figure legend, the reader is referred to the web version of this article.)

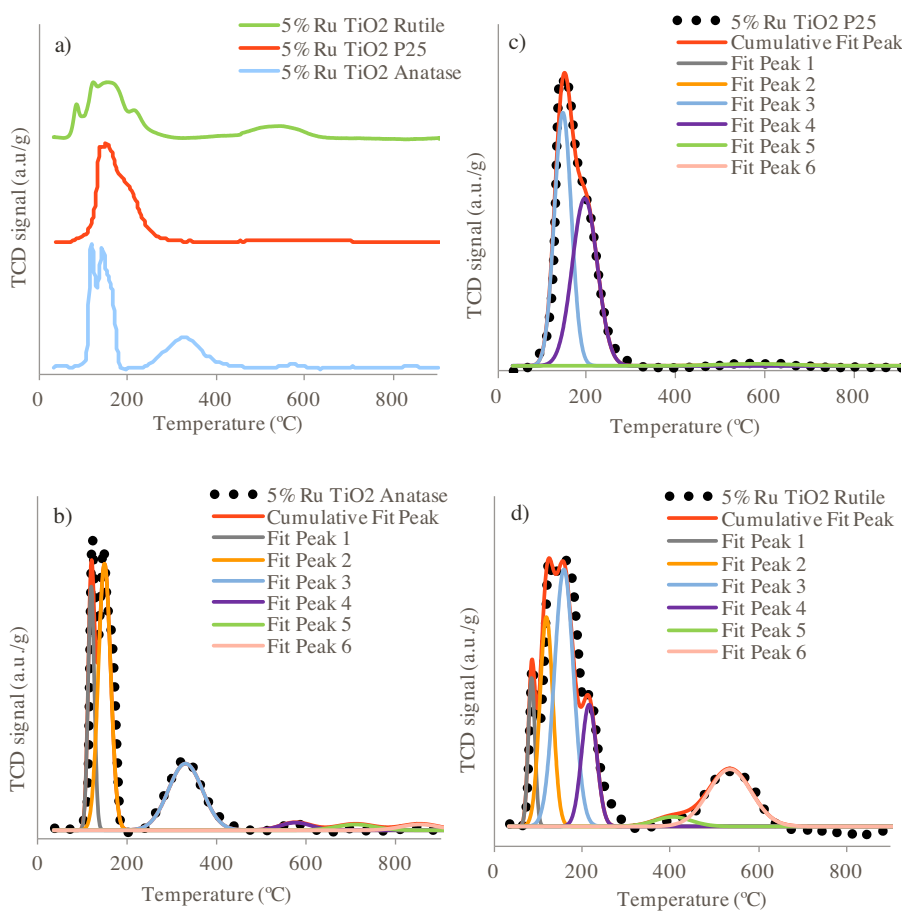


Fig. 5. Temperature programmed reduction (TPR) of 5% wt. Ru supported on TiO₂ anatase (a) (blue), TiO₂ P25 (red), and TiO₂ rutile (green). (For interpretation of the references to color in this figure legend, the reader is referred to the web version of this article.)

Table 4

Hydrogen consumption and extent of reduction of RuO₂ and TiO₂ species during temperature programmed reduction for the different catalysts.

| Catalyst | H ₂ consumption | | % of RuO ₂ Reduced | % of TiO ₂ reduced |
|--------------------------------|---|---|-------------------------------|-------------------------------|
| | (μmol of H ₂ /g) | (μmol of H ₂ /m ²) | | |
| 5% Ru TiO ₂ Anatase | 527.1 | 5.7 | 100% | 20% |
| 5% Ru TiO ₂ P25 | 196.7 | 4.2 | 100% | 24% |
| 5% Ru TiO ₂ Rutile | 457.7 | 18.3 | 100% | 35% |

increased from anatase, P25 to rutile, with values of 20%, 24%, and 35% reduction.

Similar observations have been reported by J.E. Rekoske and M. A. Barteau when studying the rates of reduction of polymorph TiO₂ anatase and rutile under isothermal conditions [63]. In that case a difference of 2.5 time larger rates of surface reduction were obtained on rutile compared to anatase. The differences were attributed to higher concentration of Ti cation on low index planes of TiO₂ rutile. DFT studies on the reducibility of TiO₂ rutile and anatase crystals showed that the less dense structure of anatase distortions the octahedron inducing a lift of degeneracy of the lowest Ti levels favouring the formation of a low spin state. As a result, TiO₂ anatase is less reducible than rutile [64]. Furthermore, the addition of H–H dissociation catalyst enhances the reducibility of TiO₂. J.E. Rekoske and M. A. Barteau demonstrated through kinetic fitting that addition of ruthenium changed the rate limiting step that controlled the reduction process. On bare TiO₂ surface, i.e. without ruthenium, the rate limiting step was the interaction between the surface O atom and the H atom adsorbed on the surface. In contrast, when ruthenium was present the rate controlling step was the replacement of the surface O by oxygen from the bulk. They proposed that the role of ruthenium was the homolytic dissociation H–H that quickly spill-over the TiO₂ surface. These observations were in line with DFT calculations of H–H dissociation on Ru–TiO₂ anatase. The results showed that in the presence of sufficient hydrogen it is thermodynamically favourable to transfer hydrogen to the metal oxide (TiO₂ anatase) with the corresponding electron transfer to the empty states of the support reducing the oxide [66].

Furthermore, the strong interaction of Ru and TiO₂ changes the electronics of the surface. A recent X-Ray photoelectron spectroscopy (XPS) study of TiO₂/C has shown the electronic properties of TiO₂ are significantly modified in the presence of Ru nanoparticles [20]. Upon addition of Ru a shift to lower binding energies of approximately 1 eV was observed on the Ti 2p^{3/2} peak, suggesting that Ti cations have become electron enriched. This “partial reduction” was tentatively attributed to an electronic effect from Ru. Ex-situ reduction of the catalyst prior XPS characterization further shifted the Ti 2p^{3/2} to even lower binding energies, which indicated the reduction of Ti⁴⁺ to Ti³⁺ [49,67]. These electronic effects are strongly affected by the catalyst dispersion. G. Haller and D. E. Resasco demonstrated that it is possible to achieve a higher degree of metal-support interaction by increasing metal dispersion [68]. They observed that on reduced Rh/TiO₂ and Ir/TiO₂ catalysts prepared by ion-exchange technique, with metal dispersions of nearly 100%, the catalytic activity towards isomerization and dehydrogenation of alkanes were unusually higher than those observed on catalysts supported on inert metal oxides (e.g. SiO₂) or catalysts prepared using conventional impregnation technique on TiO₂. It is possible to associate the higher concentration of partially unsaturated Ti³⁺ to a higher degree of TiO₂ reduction caused by the greater metal dispersion. The same observation has been reported by electron paramagnetic resonance (EPR) and X-ray photoelectron spectroscopy (XPS) when Pt and Ru supported on CeO₂ and TiO₂ were pre-reduced in H₂ [22,63,69].

Therefore, the differences in H₂ uptake per surface area and extent of reduction observed between Ru/TiO₂ rutile and anatase could be due to a combination of factors. One hand, the higher reducibility of rutile TiO₂ caused by the larger surface density of metal cations and anions on rutile low index planes that accelerates the rate of reduction and on the other the higher dispersion of Ru clusters that increases the hydrogen spill-over and the degree of metal-support interaction.

3.1.6. Ammonia temperature programmed desorption (NH₃-TPD)

Temperature programmed desorption experiments of ammonia (NH₃-TPD) was employed to determine the concentration of acid

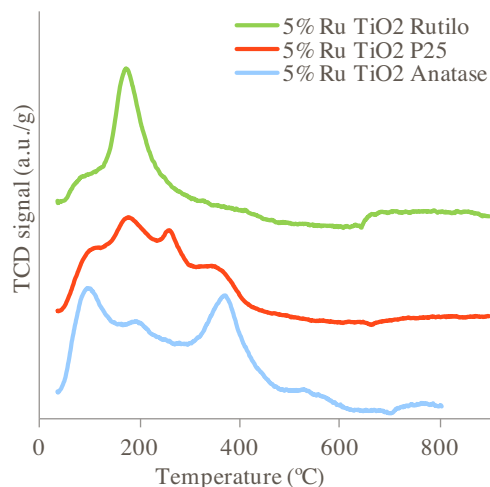


Fig. 6. Temperature programmed desorption of ammonia of 5% wt. Ru supported on TiO₂ anatase (blue), TiO₂ P25 (red), and TiO₂ rutile (green). (For interpretation of the references to color in this figure legend, the reader is referred to the web version of this article.)

Table 5

Acid site density per surface area and mass of catalyst.

| Sample | Acid site density (μmol NH ₃ /m ²) | Acid site density (μmol NH ₃ /g) |
|--------------------------------|---|---|
| 5%/Ru/TiO ₂ Anatase | 5.47 | 503 |
| 5%/Ru/TiO ₂ P25 | 11.73 | 551 |
| 5%/Ru/TiO ₂ Rutile | 12.48 | 312 |

sites in the catalyst. Fig. 6 shows the results of TPD for the three Ru/TiO₂ catalysts in stacked format for clarity. The desorption of NH₃ starts in the three catalysts at temperatures ranging 80–100 °C. While it is possible to use the desorption temperatures of NH₃ to infer the strength active sites the possible interference of other phenomena hinders the utilization of this technique to obtain energetic parameters. The studies reported by R. J. Gorte have shown that in fact when characterizing catalytic materials such as high-surface area zeolites and metal oxides it is possible that mass transport limitations and adsorbate-adsorbate interactions can lead to shifts in the temperature programmed desorption profiles of probe molecules [70,71]. His studies demonstrated that it is not possible to obtain energetic information from TPD techniques. Instead, he proposed that the only information that can be gathered from TPD are the total concentration of active sites, surface reaction mechanisms, and gas phase products. Similar conclusions were reported by S. Kouva et al. [72] for TPD-NH₃ performed on aluminosilicates. Here, it is important to keep in mind that these conclusions were drawn from the analysis of TPD-NH₃ data obtained from high-surface area zeolites, where significant intra-particle diffusion limitations and adsorbate-adsorbate repulsion interactions can lead to significant shifts in the desorption temperature [72]. However, on metal oxides with macro- and meso- porosity, like the ones employed in the present study, the intra-particle diffusional limitations are significantly reduced [73]. Therefore, the only possible cause of any deviation in the desorption temperatures can be due to adsorbate-adsorbate interactions. For this reason, it is rather difficult to obtain valid conclusions regarding the strength of the acid sites present on the materials herein studied. Instead, the total acid site density has been calculated (see Table 5).

As shown in Table 5 the total acid site concentration per mass of catalyst was significantly larger on Ru/TiO₂ P25 (551 μmol NH₃/g) and anatase (503 μmol NH₃/g), compared to rutile (312 μmol NH₃/g). This is due to the larger specific surface areas of TiO₂ P25

and anatase that provide a higher concentration of active sites in terms of catalyst mass. However, when the acid site density was expressed in terms of surface area rutile and P25 showed the highest values, respectively. These results are in line with the temperature programmed reduction results, where rutile had the largest H₂ uptake per surface area compared to anatase. This result will be in line with temperature programmed reduction data. The higher metal dispersion of Ru clusters and the more reducible nature of TiO₂ rutile are responsible for the larger concentration of acid sites and H₂-uptake per surface area.

3.2. Ketonization results

3.2.1. Effect of reaction time and temperature

Acetic acid ketonization reactions were carried out over the three catalysts prepared, at different reaction times and temperatures, in aqueous or organic reaction medium. As a benchmark, we used *n*-hexane to measure the reaction kinetics at different temperatures to avoid competitive adsorption between acetic acid and the solvent. Previous work published by C. K. Lee et al. [74] showed that heat of adsorption of organic molecules on TiO₂ nanotubes materials strongly depends on the polarity of the probe molecule. The results indicated that the heat of adsorption progressively increased with the polarity of the adsorbate. In a recent report T. Pham et al. [22] showed that on Ru/TiO₂/C water, CO₂ and acetone compete with acetic acid for the active sites. The heat of adsorption obtained by fitting a Langmuir-Hinshelwood kinetic model for water, CO₂ and acetone were –81.80, 109.73, and –87.54 kJ/mol, respectively. While these values were significantly smaller than the one of acetic acid (–133.97 kJ/mol) these products bound sufficiently stronger with the surface to compete with acetic acid for the active sites.

The results of acetic acid conversion at different reaction times (up to 8 h) and different temperatures (200, 210 and 220 °C) in *n*-hexane are presented in Fig. 7. At 200 °C, for all the catalysts the conversion initially increased rapidly up to 10% for rutile catalyst (Fig. 7a), and 20% for P25 and anatase catalysts (Fig. 7b and c). However, after 2 h of reaction the conversion reached a plateau for all the catalysts. It has been reported that in the ketonization of acetic acid in vapor phase over Ru/TiO₂, acetone and water competitively adsorb on the catalyst surface [24], which could explain the decrease in the reaction rate as the concentration of water and acetone increases with reaction time. It is important to mention that competitive adsorption effects could be accentuated when polar solvents are employed. These effects have been reported previously by S. Mukherjee and M. A. Vannice [75,76], in liquid phase hydrogenation of citral on palladium supported on silica catalyst on solvent with different physical and electronic properties.

Intrinsic catalytic activities of the different catalysts were attained employing the ketonization data and acid site density. Assuming that each ammonium adsorbate binds to two acid sites and assuming that the majority of the acidity of the catalyst between is caused by exposed Ti cations on the surface that can act as active sites in the decarboxylative ketonization, it is possible to determine the TOF of each catalyst [77]. Table 6 summarizes the values of TOF calculated at short reaction times at 200, 210, and 220 °C, for the three catalysts. Notably, the TOF increased for anatase, P25, and rutile as function of reaction temperature.

This trend indicates that in the case of rutile the intrinsic kinetic rates for the acetic acid ketonization are nearly two times faster compared to anatase. Although, there is a lower concentration of acid sites per mass of catalyst on 5 wt.% Ru/TiO₂ rutile the reaction rate per site is always larger compared to the other two catalysts. To rationalize these differences in intrinsic activity one should consider the possible electronic and structural effects of Ru on TiO₂ rutile and anatase. Metal support interactions between Ru clusters

Table 6

Turn over frequencies of the different catalysts for the decarboxylative coupling of acetic acid in *n*-hexane (liquid-phase) obtained on 5 wt.% Ru supported on TiO₂ anatase, P25 and rutile. The turn over values were determined using the total surface sites obtained by NH₃-TPD.

| Catalyst | Temperature (°C) | TOF (s ⁻¹) |
|--------------------------------|------------------|------------------------|
| 5% Ru TiO ₂ Anatase | 220 | 0.13 |
| 5% Ru TiO ₂ P25 | | 0.15 |
| 5% Ru TiO ₂ rutile | | 0.23 |
| 5% Ru TiO ₂ Anatase | 210 | 0.11 |
| 5% Ru TiO ₂ P25 | | 0.09 |
| 5% Ru TiO ₂ rutile | | 0.18 |
| 5% Ru TiO ₂ Anatase | 200 | 0.01 |
| 5% Ru TiO ₂ P25 | | 0.03 |
| 5% Ru TiO ₂ rutile | | 0.04 |

an TiO₂ could lead to electronic modification on Ti and Ru [20]. For instance, combined experimental and theoretical calculation studies of density of states (DOS), Hirshfeld charge analysis, and electron deformation density (EDD) demonstrated that during the oxidation of CO the higher activity observed on Ru-TiO₂ was largely due to the lower activation energies. The results were attributed to the electron charge transfer from the Ru to TiO₂. This metal-support interaction was mainly localized at the interface of Ru-TiO₂ via the Ru-O bond. Similar results have been reported by Bell et al. [78] were the specific activity and selectivity of the catalyst for the Fischer-Tropsch reaction was dominated by the interface between Ru and TiO₂. In those examples Ru was directly involved in the reaction mechanism stabilizing surface reaction intermediates that were kinetically relevant for the CO oxidation and Fischer-Tropsch reactions. However, in the case of decarboxylative ketonization the partially unsaturated cations are believed to be the active sites for the stabilization of the carboxylates intermediates that subsequently decompose to form ketones, water and carbon dioxide. While the exact surface reaction mechanism is still a matter of debate, it has been shown that the most plausible mechanism involves a bi-molecular coupling of two carboxylate species to form a β-ketoacid intermediate [15,22]. Thus, it is not entirely clear if the interface Ru-TiO₂ is the controlling parameter for the ketonization. Instead, H–H spillover on the Ru-TiO₂ is a more plausible explanation for such marked changes in surface reducibility, acidity, and catalytic activity observed when Ru is added to TiO₂ [15,20,24,63]. In a recent publication, G. Pacchioni [23] presented a comprehensive revision with a DFT perspective of the ketonization of carboxylic acids over TiO₂ and ZrO₂ surfaces. In this revision it was shown that the role of reducible metals supported on TiO₂ and ZrO₂ is still not well understood. The simple H-spill-over is just one of the possible roles of the metal clusters on TiO₂, but many other possible interactions could be also present in the system that can be controlling the surface reaction, including; defect migration and stabilization by metal clusters, formation of oxide nanoclusters, or encapsulated core-shell structures, and interstitial stabilization of metal atoms inside the metal oxide framework [79,80]. In this scenario, structural effects can play a more decisive role. For instance, M. A. Barteau demonstrated employing simply electrostatic theory analysis that on TiO₂ rutile (110) and anatase (001) coordinatively unsaturated Ti⁴⁺ cations are more reducible on TiO₂ rutile than anatase. The results indicate that on TiO₂ rutile the intrinsic Lewis acidity of Ti⁴⁺ cations at the (110) is higher than that of the metal cations in anatase (001) planes [81]. Also, the distances between Ti cations varies substantially with the crystalline structure. For instance, the number of next-nearest Ti atoms on anatase is 2, compared to rutile with 10 nearest atoms at Ti-Ti distances of 2.96 (2) and 3.57 Å (10) [64]. As a result, the distance of two surface Ti cations is reduced substantially. As a result, it is possible to reduce the intermolecular distance between surface carboxylates. This is

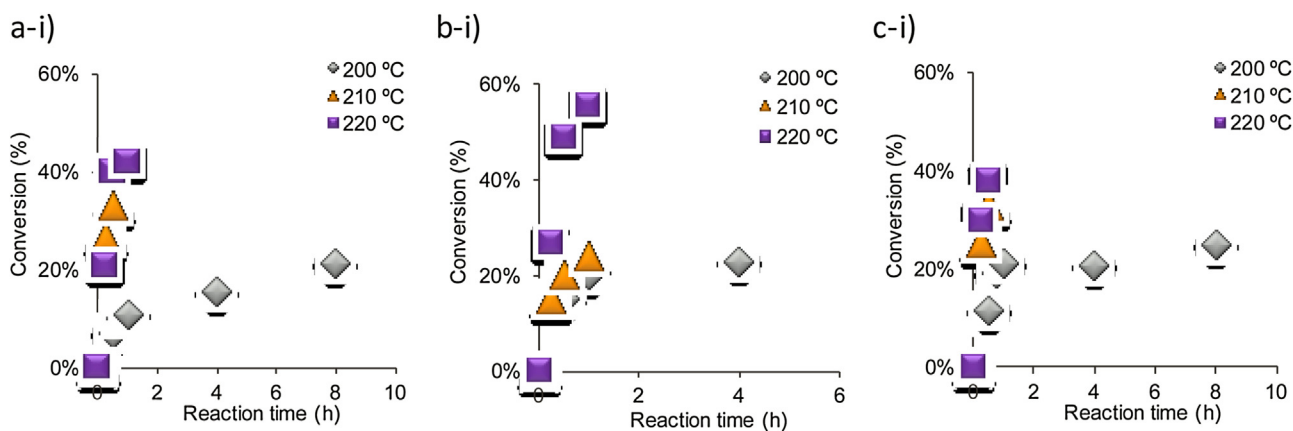


Fig. 7. Acetic acid conversion as function of time for the decarboxylative coupling in liquid *n*-hexane at 200 °C, 210 °C, and 220 °C on 5 wt.% Ru supported on TiO₂ rutile (a), P25 (b), and anatase (c).

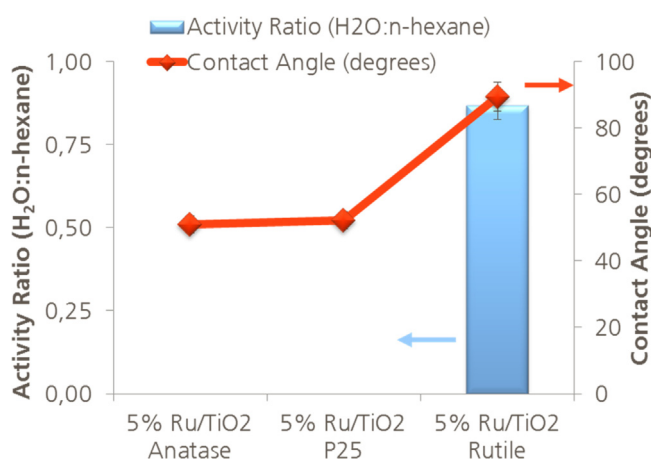


Fig. 8. Ratio of acetic acid conversion in liquid phase H₂O:*n*-hexane (blue bars) over 5 wt.% Ru supported on TiO₂ anatase, P25, and rutile after 1 h of reaction at 220 °C, 750 rpm, and 90 bar of N₂ in the presence of 200 mg of catalyst and 1.75 M of acetic acid dissolved in 35 mL of solvent. The catalyst was reduced in-situ at 230 °C, 750 rpm, and 30 bar of H₂ in 35 mL of solvent for 3 h. Contact angle of the solid-H₂O-air interface of the different catalysts (red line). (For interpretation of the references to color in this figure legend, the reader is referred to the web version of this article.)

particular important as recent kinetic data of acetic acid ketonization has shown that the rate limiting step in this reaction is the surface coupling of two carboxylate species [82]. Thereby, one can imagine that reducing the interatomic distances between surface cations could ease the formation of the coupling product.

3.2.2. Aqueous vs. organic phase ketonization

In order to study the effect of the solvent on the reaction, experiments on aqueous phase were performed at 220 °C for 1 h to compare with the results obtained under the same conditions with *n*-hexane as solvent.

To determine the stability of these catalysts in aqueous environment, the ratio of catalytic activity per gram of catalyst for the ketonization of acetic acid was determined for the three catalysts in *n*-hexane and water (Fig. 8). Here, it was observed that on 5 wt.% Ru TiO₂ anatase and P25 the ratio of activity in water: *n*-hexane was zero, while in the case of rutile this value was 0.87. This indicates that on 5 wt.% Ru/TiO₂ rutile the catalytic activity in water was nearly the same as in *n*-hexane, while in anatase and P25 the activity was negligible. It has been proposed that in the presence of condensed water at high temperatures fast deactivation of metal oxides takes place due to the structural collapse [27]. On

zeolites the presence of defectives sites, typically OH-metal moieties, determines the stability of the crystalline structure in hot liquid water [34,35]. In addition, the water molecules formed in the reaction compete with acetic acid for the active sites of the catalyst, what could be more acute on more hydrophilic surfaces [83].

It has been reported that the absence of structural defects or hydroxyl functional groups changes the surface wettability, making it more hydrophobic [84,85]. Therefore, one could use the contact angle as an indirect measurement of the surface hydroxyl groups or defects on metal oxides. To determine the contact angle of the different powders we employed the technique developed by Teipel and Mikonsaari [85] based on Washburn's equation [86]. The contact angles resulting from the water-*n*-hexane penetration experiments allow the determination of the average surface wettability. All the TiO₂ samples were previously calcined to 400 °C. Figs. S2 and S3 present the mass ratio of water adsorbed per mass of sample as function of time for TiO₂ anatase, P25, and rutile. The results indicated that on TiO₂ anatase it is possible to adsorb a large amount of water quickly (~1.5 gH₂O/g_{sample} in 400 s), while on TiO₂ rutile the mass of water and rate of adsorption were significantly smaller (~0.4 gH₂O/g_{sample} in 1766 s). As a result, the liquid-solid-gas contact angle of anatase and rutile were 51.0 and 89.5°, respectively (see Fig. 8). These values are in line with previous reports on TiO₂ freshly cleaved rutile (110) [36]. Interestingly, on P25 the behavior was intermediate between anatase and rutile. The mass absorbed was slightly higher than the one observed on anatase (~1.7 gH₂O/g_{sample} in 1766 s), but the profile was significantly different. In this sample, it was possible to identify two different regions of adsorption before saturation.

Considering that the contact angle is a function of the kinetic rate of water adsorption, which in the case of P25 changes significantly with time, it is difficult to calculate a single contact angle. As an alternative, we calculated the contact angle using the two sections of the curve. As a result, we obtained a contact angle of 89.5 and 43° for section 1 and 2 of the curve, respectively. These two contact angles resembled that of anatase and rutile, indicating that on P25 there are domains with high hydrophilicity and hydrophobicity. If one assumes that the contact angle of the mixed surface behaves like a physical mixture of rutile and anatase one can calculate the average contact angle as a linear combination of the two crystalline oxides at a ratio 80:20 anatase:rutile. This results in a contact angle of 52.29°. One can immediately recognize that the hydrophilicity of anatase dominates explaining the similarities in performance of 5wt. Ru on TiO₂ supported on P25 and anatase in aqueous phase.

The low activity of the more hydrophilic catalysts (5 wt.% Ru TiO₂ anatase and P25) compared to rutile could be due to either strong competition of water molecules on more hydrophilic TiO₂ anatase and P25 or the structural collapse of the porous structure of the catalyst. Previous studies from D. E. Resasco have shown that in zeolites the stability in condensed water at high temperatures (>150 °C) is controlled by the concentration of structural defects on the lattice of the crystal [31,32]. These defects are typically OH-terminated, which confers a hydrophilic character to these materials. Functionalization of these hydroxyl groups with organosilanes stabilizes the defects preventing the hydrolytic cleavage of the Si–O–Si bonds, while making the catalyst hydrophobic [16]. The hydrophobicity per se is not what prevent the deactivation, but rather the neutralization of highly reactive defects on the zeolite structure. While it is possible that the higher hydrophobicity of Ru/TiO₂ rutile could indicate a lower concentration of OH- groups or defects, at present there is no direct evidence to support it. Furthermore, if one considers that in terms of surface area Ru/TiO₂ rutile contains nearly 2 times more surface acid sites and 3 times higher surface hydrogen uptake, which are closely related to partially unsaturated Ti cations or defects, then it is more difficult to rationalize the stabilization solely based on the concept of density of surface defects or OH- groups.

Alternatively, it is possible that strongly bound water molecules to highly hydrophilic TiO₂ anatase and P25, blocking the adsorption sites for the formation of surface acetates, which are the precursors of ketonization products [19,21,67,87,88]. It has been showed that on TiO₂ anatase water molecules dissociatively adsorb on partially unsaturated Ti cations. The results showed that on surface oxygen vacancies H₂O dissociates through the transfer of one proton to a nearby oxygen atom, forming two hydroxyl groups for every vacancy [28]. Therefore, one could expect that on a partially reduced surface, like the ones herein reported, with a high concentration of unsaturated Ti cations, quick saturation of the surface by OH- groups should take place upon exposure to condensed water. While having a higher density of surface unsaturated Ti cations will most likely result in a higher hydrophilicity upon water exposure, it is important to mention that this is a reversible process. For instance, detailed single-crystal studies reported by R. Wang et al. [36] revealed that TiO₂ wettability can reversibly switch from hydrophobic to superhydrophilic upon exposure to UV-light. Initially, TiO₂ freshly cleaved (rutile) (110) showed a contact angle of 74° and upon 30 min exposure to 40 mW/cm² the contact angle decreased to zero degrees. More importantly, on polycrystalline anatase this switch was more easily achieved with light intensities as low as 0.1 mW/cm² and a much shorter time of UV illumination. The change in surface wettability was attributed to the formation of surface hydroxyl groups on Ti³⁺ cations, generated by the UV-Light, creating hydrophilic moieties that increased water-wettability. More recently, X. Feng et al. [37] reported that on TiO₂ rutile nanorods films it is possible to achieve switchable superhydrophobicity as a result of the combination of micro- and nanoscale hierarchical surface structures, the orientation of the crystal planes, and the surface photosensitivity. In a recent publication K.K. Varanasi demonstrated the electronic configuration of the metal cations at the outer layer could also influence the Hydrophilic-Lipophilic balance (HLB) of the surface [89]. Here, it was reported that in rare earth metal oxides, the electronic orbitals that can serve as H-bonding sites for water molecules, i.e. the unfilled 4f orbitals are shielded from interactions with the surrounding environment by the full octet of electrons in the 5s²6p⁶ outer shell. In the alumina, however, aluminium atoms are electron-deficient, with six electrons in their three sp²-hybrid orbitals, which favour the formation of H-bonding with interfacial water molecules. If one compares the electronic structure of Al³⁺ and Ti⁴⁺ one can immediately recognize that in both cases the sp²-

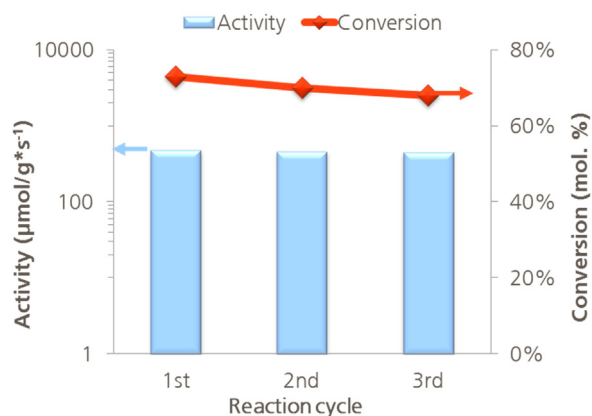


Fig. 9. Recyclability of the 5 wt.% Ru supported on TiO₂ rutile after several reactions in aqueous phase at 200 °C: Catalytic activity of the catalyst (mol/g*s⁻¹) (blue bars) and conversion of acetic (red line). (For interpretation of the references to color in this figure legend, the reader is referred to the web version of this article.)

hybrid orbitals contain six electrons. Therefore, one should expect TiO₂ to be inherently hydrophilic. However, that is not the case for TiO₂ rutile.

The exact nature of the stability of TiO₂ rutile supported catalysts is still not entirely clear. The experimental evidence indicates that surface hydrophobicity is critical for the stability in hot liquid water, but the true nature of the phenomena requires additional studies. Elucidating the exact mechanism of stabilization will be critical for the development of metal oxides with high-stability for reactions in hot liquid water.

3.2.3. Catalyst recyclability

Finally, to demonstrate the enhanced stability of the 5 wt.% Ru supported on TiO₂ rutile a series of reaction with recycled catalyst was performed. Fig. 9 presents the catalytic activity after several reaction cycles employing water as reaction solvent. Notably, the catalytic activity and conversion remained unaltered after three reaction cycles with values of 483, 463, and 450 μmol/g*s⁻¹. The higher hydrothermal stability of the rutile supported catalyst could be tentatively attributed to surface hydrophobic character [32]. This can be inferred from fact that rutile formation requires the thermal treatment of TiO₂ to temperatures above 600 °C [90], where significant surface dehydroxylation occurs [91]. Also, one could attribute the higher stability in hot condensed water to the thermodynamic stability of TiO₂ rutile compared to anatase [92]. In many synthesis methods the initial crystalline TiO₂ formed in generally anatase. This can be attributed to the lower energetic barriers for the arrangement of short-range ordered TiO₆ octahedra into long-range anatase during synthesis [93]. Thus, it is possible that under the proper reaction conditions the reversed synthesis process, i.e. dissolution and amorphization, could take place more easily on anatase than rutile. However, at this point additional studies are required to identify the controlling parameters of the enhanced stability of 5 wt.% Ru/TiO₂ rutile.

4. Conclusions

Liquid phase acetic acid ketonization reactions have been studied on Ru catalysts supported on three different TiO₂ (anatase, rutile and a mixture of rutile: anatase). The combination of the lattice matching effect between the rutile phase of ruthenium oxide and TiO₂, followed by thermal treatment, enhanced both catalytic activity and hydrothermal stability without the need of any surface functionalization by organosilanes. This resulted in faster reaction rates compared to the same catalysts based on P25 and anatase.

The rutile hydrophobicity improved the stability of the Ru-TiO₂ rutile catalyst, resulting in negligible losses in catalytic activity after several reaction cycles in aqueous phase. While the true nature of the stability in hot liquid water remains elusive the impact of the surface Hydrophilic-Lipophilic balance (HLB) is clearly. To properly describe the surface wettability of TiO₂ and, more importantly, the enhanced stability of Ru/TiO₂ rutile in aqueous phase at high temperatures further studies are required. Achieving this goal will require the study of all the parameters influencing the surface wettability of TiO₂ and its stability in hot condensed water, including; porosity, crystalline structure, nano- and micro- scale architecture, electronic structure, surface chemistry, as well as the possible blocking towards the active sites caused water competitive adsorption. We envision that the concept of combining lattice matching effects and surface hydrophobization on Ru-TiO₂ could be extrapolated to other materials for applications as diverse as high-temperature photocatalysis, thermochemical water splitting, commodity chemical synthesis (e.g. HCl oxidation), and biomass conversion, where hydrothermal stability of the catalyst is critical for the process economic viability.

Acknowledgements

This work was funded by Abengoa Research and the European Union Seventh Framework Programme (FP7/2007–2013) under grant agreement no. 604307. The authors would like to thank Dr. J.C. Serrano, Dr. M. A. Díaz, and Dr. J. Arauzo their helpful discussions, Dr. G. Rincón for the help with XRD and Contact Angle Measurements. We thank Dr. D. E. Resasco for helpful discussions on liquid phase ketonization and hydrothermal stability.

Appendix A. Supplementary data

Supplementary data associated with this article can be found, in the online version, at <http://dx.doi.org/10.1016/j.apcata.2016.10.025>.

References

- [1] H. Röper, *Starch-Stärke* 54 (2002) 89–99.
- [2] N. Tanaka, *Technology Roadmap: Biofuels for Transport*, Paris, 2011.
- [3] G.W. Huber, S. Iborra, A. Corma, *Chem. Rev.* 106 (2006) 4044–4098.
- [4] A. Corma Canos, S. Iborra, A. Velty, *Chem. Rev.* 107 (2007) 2411–2502.
- [5] D.E. Resasco, S. Crossley, *AIChE J.* 55 (2009) 1082–1089.
- [6] D.E. Resasco, S.P. Crossley, *Catal. Today* 257 (2015) 185–199.
- [7] J.C. Serrano-Ruiz, J.A. Dumesic, *Energy Environ. Sci.* 4 (2011) 83–99.
- [8] A.V. Bridgwater, *Biomass Bioenergy* 38 (2012) 68–94.
- [9] M. Ringer, V. Putsche, J. Scahlil, *Large-Scale Pyrolysis Oil Production: A Technology Assessment and Economic Analysis*, Golden, 2006.
- [10] S. Xiu, A. Shahbazi, *Renew. Sustain. Energy Rev.* 16 (2012) 4406–4414.
- [11] D. Mohan, C.U. Pittman, P.H. Steele, *Energy Fuels* 20 (2006) 848–889.
- [12] J. Piskorz, D.S. Scott, D. Radlein, *ACS Symp. Ser. Am. Chem. Soc.* (1988) 165–178.
- [13] J.H. Marsman, J. Wildschut, P. Evers, S. de Koning, H.J. Heeres, J. Chromatogr. A 1188 (2008) 17–25.
- [14] S. Czernik, A.V. Bridgwater, *Energy Fuels* 18 (2004) 590–598.
- [15] T.N. Pham, T. Sooknoi, S.P. Crossley, D.E. Resasco, *ACS Catal.* 3 (2013) 2456–2473.
- [16] P.A. Zapata, J. Faria, M.P. Ruiz, R.E. Jentoft, D.E. Resasco, *J. Am. Chem. Soc.* 134 (2012) 8570–8578.
- [17] T.N. Pham, D. Shi, D.E. Resasco, *Appl. Catal. B: Environ.* 145 (2014) 10–23.
- [18] K.S. Kim, M.A. Barteau, *J. Catal.* 125 (1990) 353–375.
- [19] K.S. Kim, M. a Barteau, *Langmuir* 6 (1990) 1485–1488.
- [20] T.N. Pham, D. Shi, T. Sooknoi, D.E. Resasco, *J. Catal.* 295 (2012) 169–178.
- [21] O. Nagashima, S. Sato, R. Takahashi, T. Sodesawa, *J. Mol. Catal. A: Chem.* 227 (2005) 231–239.
- [22] T.N. Pham, D. Shi, D.E. Resasco, *J. Catal.* 314 (2014) 149–158.
- [23] G. Pacchioni, *ACS Catal.* 4 (2014) 2874.
- [24] T.N. Pham, D. Shi, D.E. Resasco, *Top. Catal.* 57 (2013) 706–714.
- [25] C.A. Gaertner, J.C. Serrano-Ruiz, D.J. Braden, J.A. Dumesic, *J. Catal.* 266 (2009) 71–78.
- [26] R.W. Snell, B.H. Shanks, *ACS Catal.* 3 (2013) 783–789.
- [27] R.M. Ravenelle, F. Schübler, A. Damico, N. Danilina, J.A. Van Bokhoven, J.A. Lercher, C.W. Jones, C. Sievers, *J. Phys. Chem. C* 114 (2010) 19582–19595.
- [28] R. Schaub, N. Lopez, I. Stensgaard, J.K. Norskov, F. Besenbacher, *Phys. Rev. Lett.* 87 (2001) 266104–1–266104-4.
- [29] Z. Wang, X. Hao, S. Gerhold, Z. Novotny, C. Franchini, E. McDermott, K. Schulte, M. Schmid, U. Diebold, *J. Phys. Chem. C* 117 (2013) 26060–26069.
- [30] U. Diebold, *Surf. Sci. Rep.* 48 (2003) 53–229.
- [31] P.A. Zapata, Y. Huang, M.A. Gonzalez-Borja, D.E. Resasco, *J. Catal.* 308 (2013) 82–97.
- [32] L. Zhang, K. Chen, B. Chen, J.L. White, D.E. Resasco, *J. Am. Chem. Soc.* 137 (2015) 11810–11819.
- [33] Y. Román-Leshkov, M. Moliner, J.A. Labinger, M.E. Davis, *Angew. Chem. Int. Ed.* 49 (2010) 8954–8957.
- [34] A. Corma, L.T. Nemeth, M. Renz, S. Valencia, *Nature* 412 (2001) 423–425.
- [35] R. Gounder, M.E. Davis, *J. Catal.* 308 (2013) 176–188.
- [36] R. Wang, N. Sakai, A. Fujishima, T. Watanabe, K. Hashimoto, *J. Phys. Chem. B* 103 (1999) 2188–2194.
- [37] X. Feng, J. Zhai, L. Jiang, *Angew. Chem. Int. Ed.* 44 (2005) 5115–5118.
- [38] J. Diebold, *A Review of the Chemical and Physical Mechanisms of the Storage Stability of Fast Pyrolysis Bio-Oils*, Golden, 1999.
- [39] H. Idriss, C. Digne, J.P. Hindermann, A. Kiennemann, M.A. Barteau, *J. Catal.* 155 (1995) 219–237.
- [40] J.E. Rekoske, M.A. Barteau, *Ind. Eng. Chem. Res.* 50 (2011) 41–51.
- [41] M.A. Barteau, *Chem. Rev.* 96 (1996) 1413–1430.
- [42] A. Pulido, B. Oliver-Tomas, M. Renz, M. Boronat, A. Corma, *ChemSusChem* 6 (2013) 141–151.
- [43] E.V. Kondratenko, A.P. Amrute, M.-M. Pohl, N. Steinfeldt, C. Mondelli, J. Pérez-Ramírez, *Catal. Sci. Technol.* 3 (2013) 2555–2558.
- [44] J. Zhang, P. Zhou, J. Liu, J. Yu, *Phys. Chem. Chem. Phys.* 16 (2014) 20382–20386.
- [45] J. Xu, X. Su, H. Duan, B. Hou, Q. Lin, X. Liu, X. Pan, G. Pei, H. Geng, Y. Huang, T. Zhang, *J. Catal.* 333 (2016) 227–237.
- [46] C. Hernandez-Mejia, E.S. Gnanakumar, A. Olivos-Suarez, J. Gascon, H.F. Greer, W. Zhou, G. Rothenberg, N. Raveendran Shiju, *Catal. Sci. Technol.* 6 (2015) 577–582.
- [47] D. Teschner, G. Novell-Leruth, R. Farra, A. Knop-Gericke, R. Schlögl, L. Szentmiklósi, M. González Hevia, H. Soerijanto, R. Schomäcker, J. Pérez-Ramírez, N. López, *Nat. Chem.* 4 (2012) 739–745.
- [48] T. Omotoso, S. Boonyasuwat, S.P. Crossley, *Green Chem.* 16 (2014) 645.
- [49] G.L. Haller, D.E. Resasco, *Adv. Catal.* 36 (1989) 173–235.
- [50] H. Iddir, M.M. Disko, S. Ogut, N.D. Browning, *Micron* 36 (2005) 233–241.
- [51] H. Iddir, V. Skavys, Ö. Serdar, N.D. Browning, M.M. Disko, *Phys. Rev. B* 73 (2006) 1–4.
- [52] M.I. Larsson (12) *United States Patent*, 7,813,523 B1, 2010.
- [53] R.A.D. Betta, *J. Catal.* 34 (1974) 57–60.
- [54] K.C. Taylor, *J. Catal.* 38 (1975) 299–306.
- [55] X. Shen, L.J. Garces, Y. Ding, K. Laubernds, R.P. Zerger, M. Aindow, E.J. Neth, S.L. Suib, *Appl. Catal. A: Gen.* 335 (2008) 187–195.
- [56] J. Okal, M. Zawadzki, L. Kepiński, L. Krajczyk, W. Tylus, *Appl. Catal. A: Gen.* 319 (2007) 202–209.
- [57] G. Bergeret, P. Gallezot, *Handbook of Heterogeneous Catalysis*, 2nd ed., Wiley-VCH, Weinheim, 1997.
- [58] G. Borah, P. Sharma, *Indian J. Chem.* 50A (2011) 41–45.
- [59] B.C. Gates, *Chem. Rev.* 95 (1995) 511–522.
- [60] D. Avnir, D. Farin, P. Pfeifer, *Nature* 308 (1984) 261–263.
- [61] S. Gheorghiu, M.O. Coppens, *AIChE J.* 50 (2004) 812–820.
- [62] M.O. Coppens, G.F. Froment, *Chem. Eng. Sci.* 49 (1994) 4897–4907.
- [63] J.E. Rekoske, M.A. Barteau, *J. Phys. Chem. B* 101 (1997) 1113–1124.
- [64] A. Bouzoubaa, A. Markovits, M. Calatayud, C. Minot, *Surf. Sci.* 583 (2005) 107–117.
- [65] L.E. Briand, L. Gambaro, H. Thomas, *J. Therm. Anal.* 44 (1995) 803–821.
- [66] H.-Y.T. Chen, S. Tosoni, G. Pacchioni, *ACS Catal.* (2015) 5486–5495.
- [67] K.S. Kim, M.A. Barteau, *J. Catal.* 125 (1990) 353–375.
- [68] D.E. Resasco, G.L. Hailer, *J. Phys. Chem. B* 101 (1997) 4552–4556.
- [69] S. Ricote, G. Jacobs, M. Milling, Y. Ji, P.M. Patterson, B.H. Davis, *Appl. Catal. A: Gen.* 303 (2006) 35–47.
- [70] R.A. Demmin, R.J. Gorte, *J. Catal.* 90 (1984) 32–39.
- [71] R.J. Gorte, *J. Catal.* 28 (1996) 405–414.
- [72] S. Kouva, J. Kanervo, F. Schübler, R. Olindo, J.A. Lercher, O. Krause, *Chem. Eng. Sci.* 89 (2013) 40–48.
- [73] M.O. Coppens, *Colloids Surf. A: Physicochem. Eng. Aspects* 187–188 (2001) 257–265.
- [74] C.K. Lee, S.K. Fen, H.P. Chao, S.S. Liu, F.C. Huang, *Adsorpt. Int. Adsorpt. Soc.* 18 (2012) 349–357.
- [75] S. Mukherjee, M.A. Vannice, *J. Catal.* 243 (2006) 108–130.
- [76] S. Mukherjee, M.A. Vannice, *J. Catal.* 243 (2006) 131–148.
- [77] J.M.G. Amores, V. Sanchez Escribano, G. Ramis, G. Busca, *Appl. Catal. B: Environ.* 13 (1997) 45–58.
- [78] T. Komaya, A.T. Bell, Z. Wengsieh, R. Gronsky, F. Engelke, T.S. King, M. Pruski, *J. Catal.* 150 (1994) 400–406.
- [79] E.W. McFarland, H. Metiu, *Chem. Rev.* 113 (2013) 4391–4427.
- [80] X. Shao, S. Prada, L. Giordano, G. Pacchioni, N. Nilius, H.J. Freund, *Angew. Chem. Int. Ed.* 50 (2011) 11525–11527.
- [81] J. Woning, R.A. Van Santen, *Chem. Phys. Lett.* 101 (1983) 541–547.
- [82] J.M. Vohs, *Chem. Rev.* 113 (2013) 4136–4163.
- [83] J. Struijk, M. D'Angremond, W.J.M.L. de Regt, J.J.F. Scholten, *Appl. Catal. A: Gen.* 83 (1992) 263–295.
- [84] J. Drzymala, *Adv. Colloid Interface Sci.* 50 (1994) 143–185.
- [85] U. Teipel, I. Mikonsaari, *Part. Part. Syst. Char.* 21 (2004) 255–260.

- [86] E.W. Washburn, *Phys. Rev.* 17 (1921) 273–283.
- [87] R. Martinez, M.C. Huff, M.A. Barteau, *J. Catal.* 222 (2004) 404–409.
- [88] R. Pestman, R.M. Koster, J.A.Z. Pieterse, V. Ponec, A. van Duijne, *J. Catal.* 168 (1997) 255–264.
- [89] G. Azimi, R. Dhiman, H.-M. Kwon, A.T. Paxson, K.K. Varanasi, *Nat. Mater.* 12 (2013) 315–320.
- [90] P.S.O.F. Anatase, *Am. Mineral.* 53 (1969) 1929–1930.
- [91] D.N. Misra, *Nat. Phys. Sci.* 240 (1972) 14–15.
- [92] D.A.H. Hanaor, C.C. Sorrell, *J. Mater. Sci.* 46 (2011) 855–874.
- [93] A. Matthews, *Am. Mineral.* 61 (1976) 419–424.